



**HAL**  
open science

# Different Martian Crustal Seismic Velocities Across the Dichotomy Boundary From Multi-Orbiting Surface Waves

Jiaqi Li, Caroline Beghein, Philippe Lognonné, Scott Mclennan, Mark Wieczorek, Mark Panning, Brigitte Knapmeyer-Endrun, Paul Davis, W. Bruce Banerdt

► **To cite this version:**

Jiaqi Li, Caroline Beghein, Philippe Lognonné, Scott Mclennan, Mark Wieczorek, et al.. Different Martian Crustal Seismic Velocities Across the Dichotomy Boundary From Multi-Orbiting Surface Waves. *Geophysical Research Letters*, 2023, 50 (1), 10.1029/2022GL101243 . hal-03938829v1

**HAL Id: hal-03938829**

**<https://u-paris.hal.science/hal-03938829v1>**

Submitted on 13 Jan 2023 (v1), last revised 20 May 2023 (v2)

**HAL** is a multi-disciplinary open access archive for the deposit and dissemination of scientific research documents, whether they are published or not. The documents may come from teaching and research institutions in France or abroad, or from public or private research centers.

L'archive ouverte pluridisciplinaire **HAL**, est destinée au dépôt et à la diffusion de documents scientifiques de niveau recherche, publiés ou non, émanant des établissements d'enseignement et de recherche français ou étrangers, des laboratoires publics ou privés.

1 **Different Martian Crustal Seismic Velocities across the Dichotomy**  
2 **Boundary from Multi-Orbiting Surface Waves**

3

4 Jiaqi Li<sup>1\*</sup>, Caroline Beghein<sup>1</sup>, Philippe Lognonné<sup>2</sup>, Scott M. McLennan<sup>3</sup>, Mark Wieczorek<sup>4</sup>, Mark Panning<sup>5</sup>, Brigitte  
5 Knapmeyer-Endrun<sup>6</sup>, Paul Davis<sup>1</sup>, and William Bruce Banerdt<sup>5</sup>

6

7 <sup>1</sup> Department of Earth, Planetary, and Space Sciences, University of California, Los Angeles, CA 90095, USA.

8 E-mail: [jli@epss.ucla.edu](mailto:jli@epss.ucla.edu)

9 <sup>2</sup> Université Paris Cité, Institut de physique du globe de Paris, CNRS, Paris, F-75005, France.

10 <sup>3</sup> Department of Geosciences, Stony Brook University, Stony Brook, New York, 11794–2100 USA.

11 <sup>4</sup> Université Côte d’Azur, Observatoire de la Côte d’Azur, CNRS, Laboratoire Lagrange, Nice, France.

12 <sup>5</sup> Jet Propulsion Laboratory, California Institute of Technology, Pasadena, CA 91109, USA.

13 <sup>6</sup> Bensberg Observatory, University of Cologne, 51429 Bergisch Gladbach, Germany.

14

15

16

17

18

19

20

21

22

23

24

## 25 **Abstract**

26 We have observed both minor-arc (R1) and major-arc (R2) Rayleigh waves for the largest marsquake (magnitude  
27 of  $4.7 \pm 0.2$ ) ever recorded. Along the R1 path (in the lowlands), inversion results show that a simple, two-layer  
28 model with an interface located at 21 - 29 km and an upper crustal shear-wave velocity of 3.05 - 3.17 km/s can fit the  
29 group velocity measurements. Along the R2 path, observations can be explained by upper crustal thickness models  
30 constrained from gravity data and upper crustal shear-wave velocities of 2.61 - 3.27 km/s and 3.28 - 3.52 km/s in the  
31 lowlands and highlands, respectively. The shear-wave velocity being faster in the highlands than in the lowlands  
32 indicates the possible existence of sedimentary rocks, and relatively higher porosity in the lowlands.

## 33 **Plain Language Summary**

34 The largest marsquake ever recorded occurred recently and waves propagating at the surface, called surface waves,  
35 have been observed. Owing to the relatively large magnitude (i.e.,  $4.7 \pm 0.2$ ) of this event, surface wave energy is  
36 still clearly visible after one orbit around the red planet. The shortest path taken by the wave propagating between  
37 the source and the receiver is located in the northern lowlands, near the boundary with the southern highlands (called  
38 dichotomy). The surface wave traveling in the opposite direction, following the longer distance between the quake  
39 and the seismic station, mostly passes through the highlands. Analyses of these two paths reveal that the average  
40 shear-wave velocity is faster in the highlands than in the lowlands near the dichotomy boundary. This lower velocity  
41 in the lowlands may be due to the presence of thick accumulations of sedimentary rocks and relatively higher porosity.

42

### 43 **Key Points:**

- 44 ● Analyses of the minor-arc and major-arc Rayleigh waves reveal different Martian crustal structures across the  
45 dichotomy boundary
- 46 ● The average shear-wave velocity is faster in the highlands than in the lowlands near the dichotomy boundary.
- 47 ● The lower shear-wave velocity in the lowlands may be due to the presence of sedimentary rocks and relatively  
48 higher porosity.

# 1. Introduction

50 The InSight (Banerdt et al., 2020) mission landed a very broadband seismometer (Lognonné et al., 2019), on Mars  
51 in Nov 2018 to better understand the structure, evolution, and differentiation of the Martian crust. In nearly three and  
52 a half years, more than one thousand marsquakes and several impact events have been recorded (Clinton et al., 2021;  
53 Garcia et al., 2022; Posiolova et al., 2022). So far, multiple body-wave signals have been clearly recorded (Clinton  
54 et al., 2021), but observable surface-wave signals were only recently reported for two impact events (Kim et al.,  
55 2022).

56 Due to the lack of surface wave observations, previous seismological studies of the Martian crust and the topmost  
57 mantle were mainly based on body waves and ambient noise correlations (e.g., Lognonné et al., 2020; Knapmeyer-  
58 Endrun et al., 2021; Compaire et al., 2021; Schimmel et al., 2021; Li et al, 2022a and 2022b). Since the ray paths of  
59 the above-mentioned signals are nearly vertically incident beneath the seismometer, most of the sampled sub-surface  
60 structures are limited to the vicinity of the InSight landing site (i.e., within a radius of  $\sim 50$  km). Nevertheless, there  
61 were attempts to constrain the crustal structures at other locations (e.g., Li et al., 2022c).

62 On the 1222<sup>nd</sup> Martian day (sol) of the InSight mission, the largest marsquake (S1222a) ever recorded occurred  
63 with a magnitude of  $4.7 \pm 0.2$ , which corresponds to energy five times greater than the second-largest event  
64 (Kawamura et al. 2022; InSight Marsquake Service, 2022). For the first time, both Rayleigh and Love waves were  
65 observed on a planet other than Earth (Kawamura et al. 2022; Beghein et al. 2022; Xu et al., 2022).

66 On a radially stratified, laterally homogeneous sphere, a surface wave travels along the great-circle path. The wave  
67 that travels along the shorter path between the source and the receiver is named the minor-arc Rayleigh wave (R1).  
68 The wave that travels in the other direction, along the longer path, is named the major-arc Rayleigh wave (R2). The  
69 Rayleigh wave arrival is called R3 when the minor-arc wave circuits the globe and eventually reaches the station  
70 again. On Earth, R2 and R3 can fill the gap of poorly covered areas in tomographic models (constrained by R1 alone)  
71 and thus enhance the resolution (e.g., Trampert and Woodhouse, 1996). On Mars, the R2 and R3 observations are  
72 very important since there is only one station and thus there are lots of gaps to cover.

73 To observe the R2 and R3 Rayleigh waves, which are of much smaller amplitude than R1, the minimum moment  
74 magnitude was estimated to be Mw 6.0 for quiet stations on Earth (Panning et al., 2005). On Mars, the minimum  
75 requirement for marsquakes is between Mw 4.6 and Mw 5.3, mainly due to Mars's smaller radius (Panning et al.,  
76 2005). As predicted, the large magnitude of event S1222a enabled observations of R2 and R3 on Mars (Panning et  
77 al., 2022).

78 The epicentral distance of event S1222a is  $37.0 \pm 1.6$  degrees, and the back azimuth is estimated to be between 96  
79 and 112 degrees (Kawamura et al. 2022), placing the location of S1222a in the lowlands and near the dichotomy  
80 boundary. The dichotomy boundary separates the northern lowlands and southern highlands and has highly debated  
81 origins (Zhong and Zuber, 2001; Marinova et al., 2008; Andrews-Hanna et al., 2008; Frey, 2006). The R2 and R3  
82 Rayleigh waves pass through both the lowlands and the highlands (Fig. 1), which are far from the InSight lander and  
83 were scarcely sampled by seismic waves with the previously recorded marsquakes. These observations allow us to  
84 put new constraints on the crustal structure away from the lander in both the lowlands and the highlands.

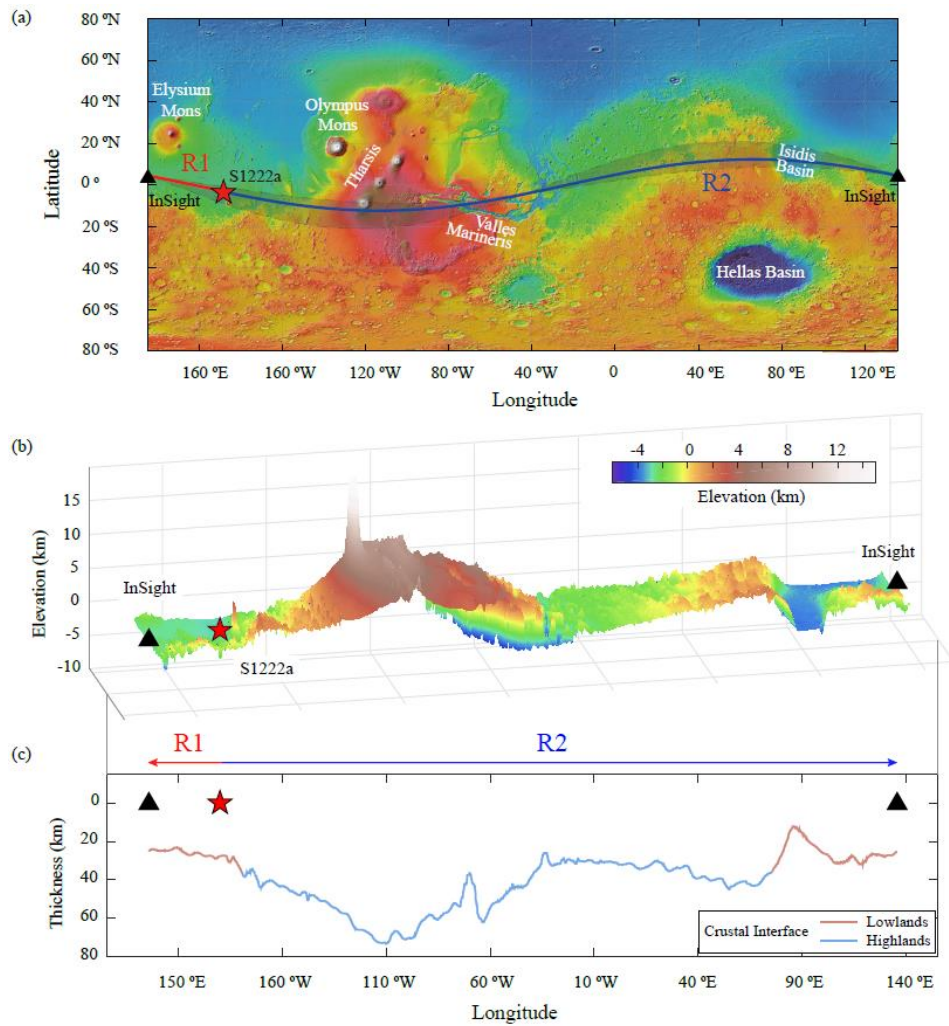
85 In this paper, we first measured the group velocity of the Rayleigh waves along the R1, R2, and R3 paths. Then,  
86 we performed inversions for R1 and R2 (the R3 measurements are less reliable, as explained below) to derive seismic  
87 velocity models that could explain the observations. After comparing the seismic velocity profiles in the lowlands  
88 and highlands, we discuss the possible effects of the crustal variations on the observed group velocities of the minor-  
89 and major-arc Rayleigh waves.

90

91

92

93



94

95

96 **Figure 1.**

97 (a) MOLA (Mars Orbiter Laser Altimeter, Smith et al., 2001) map. The red star marks the optimal hypocenter of  
 98 event S1222a (Kawamura et al., 2022), and the black triangle indicates the broadband seismometer of the InSight  
 99 mission. The red and blue curves denote the great-circle paths of R1 and R2, respectively. The shaded grey areas  
 100 illustrate all possible paths for R1 and R2 based on the back azimuth uncertainty of the event location (Kawamura  
 101 et al., 2022).

102 (b) Elevation variations along the Rayleigh wave paths shown in (a). Regions within 10 degrees of the optimal great-  
 103 circle path are displayed to account for the finite frequency effect (e.g., Zhou et al., 2004).

104 (c) Lateral variations of the upper crust along the Rayleigh wave great-circle path in (a). The depth of the interface  
 105 at the InSight lander site is fixed at 26 km from the R1 inversion (in Fig. 3c), and the relative variations are  
 106 constrained by gravity data (Wieczorek et al., 2022). The location of the dichotomy boundary is from Tanaka et  
 107 al. (2014).

108

109

110

111

## 112 **2. Data**

113 The minor arc Rayleigh wave, which travels  $2,193 \pm 95$  km (using an equatorial radius of 3396.2 km), arrives  
114 around 800 s after the origin time on the vertical component of the seismogram and can be observed over a relatively  
115 broad frequency band on both the vertical (i.e., 10 to 60 s, in Fig. 2a) and the radial components (Fig. S1). Since the  
116 seismometer is in an extremely harsh environment, the diurnal temperature variations could generate one-sided pulses  
117 (hereafter referred to as glitches) that can contaminate the seismic signals. A comparison between the raw data and  
118 the deglitched data (Scholz et al., 2020) shows that there is no significant glitch near the R1 arrival time (Fig. S1).

119 R2 travels a much longer distance of about  $19,146 \mp 95$  km and arrives around 6,650 s after the origin time (Fig.  
120 2b). R2 is observed within a relatively narrow frequency range (i.e., 25 to 35 s), and the amplitude is only about one-  
121 fourth of that of R1. Although there is no glitch near the R2 arrival, another signal of a slightly smaller amplitude  
122 occurs at about 6,800 to 7,000 s. Panning et al. (2022) excluded this signal as being the R2 phase since this later  
123 arrival does not show strong and consistent elliptical particle motions at different frequency bands (which is expected  
124 for the Rayleigh wave), and the corresponding marsquake location would be highly inconsistent with the one  
125 constrained by body waves (Kawamura et al. 2022). Therefore, we prefer selecting the R2 signal at around 6,650 s.

126 The R3 wave, which travels  $23,532 \pm 95$  km, overlaps with a glitch in the raw data (Fig. 2b). R3 is still visible on  
127 the deglitched data and exhibits arrival times of about 8,100 s. However, since the deglitching procedure may not  
128 perfectly fit the real glitch and thus could also remove some seismic signals, the R3 signals (e.g., the arrival time and  
129 amplitude) are less reliable than R1 or R2. Therefore, in the following analysis, we mainly focus on R1 and R2 and  
130 consider R3 as auxiliary data for benchmarking purposes.

131

132

133

134

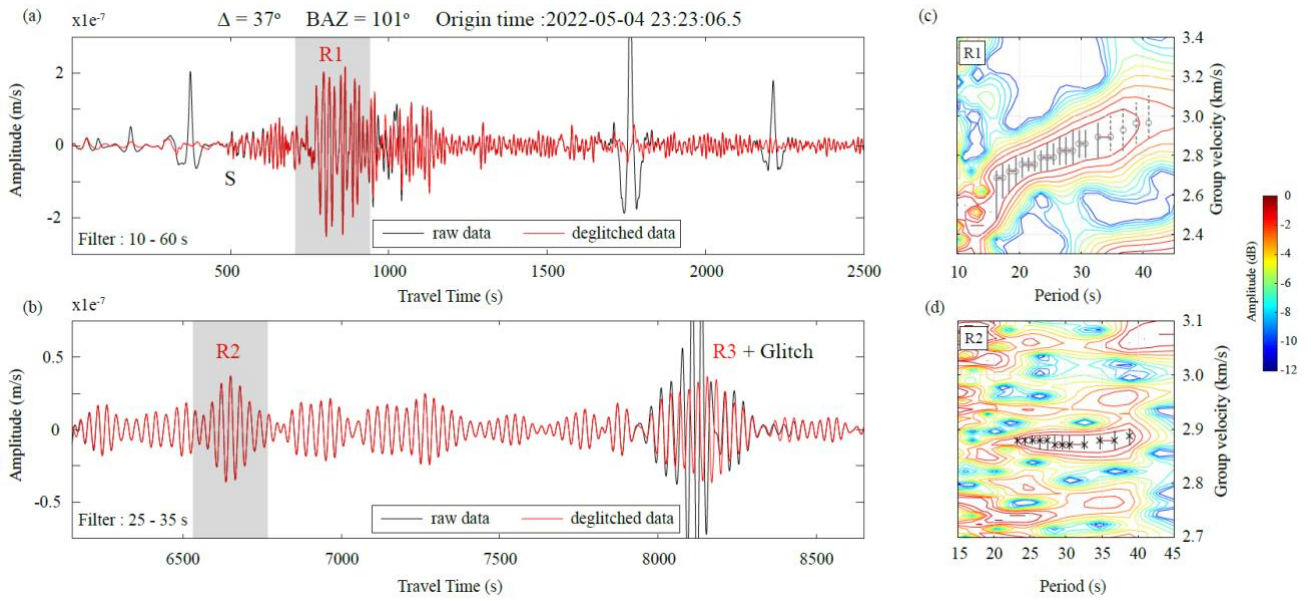
135

136

137

138

139



140

141

142 **Figure 2.**

143 (a) Seismic waveforms (after removing the instrument response and bandpass filter from 10 to 60 s) on the vertical  
 144 component near the arrival times of the S wave and R1. The black and red waveforms are the velocity records  
 145 from the raw dataset and deglitched dataset, respectively. The shaded gray region marks the time window in  
 146 which we performed the multiple filter analysis in (c).

147 (b) Waveforms on the vertical component near the arrivals of R2 and R3 with a filter band of 25 to 35 s.

148 (c) Multiple filter analysis (Herrmann, 2013) for R1 on the vertical component. The x- and y-axes are the period and  
 149 group velocity, respectively. Color scales represent the energy contours (in dB) of the waveform envelope. The  
 150 black circles indicate the preferred group velocity measurements. The vertical grey error bar spans 1 dB. Note  
 151 that at periods greater than 32 s, the R1 measurements show discrepancies between the vertical and radial  
 152 components (see Fig. S2) and thus are less reliable (denoted by the dashed error bars).

153 (d) Similar to (c) but for R2 on the vertical component.

154

155

156

157

158

159

160



## 161 **3. Method and Results**

### 162 **3.1 Group Velocity Measurements**

163 To measure the Rayleigh wave group velocity, we first performed a multiple filter analysis (Herrmann, 2013) to  
164 calculate the energy of the waveform envelope at different periods (Fig. 2c and d). Then, we selected the optimal  
165 group velocity at each period corresponding to the maximum energy (in dB) of the waveform envelope. Finally, we  
166 defined the uncertainty of the measurements using a 1dB threshold (Beghein et al., 2010), i.e., group velocities with  
167 amplitudes within 1dB of the maximum amplitude are viewed as acceptable measurements.

168 The reliable period range for the R1 signal on the vertical component is from 17 s to 32 s, where the group velocities  
169 are consistent with those measured on the radial component (Fig. S2). For the average group velocity along the R1  
170 path, there are clear signs of positive dispersion, i.e., the group velocity increases with the period. Given the origin  
171 time of 2022-05-04 23:23:06.5 (UTC) and the epicentral distance of 37 degrees (Kawamura et al. 2022), the R1 group  
172 velocity increases from  $2.70 \pm 0.05$  km/s at 17 s to  $2.95 \pm 0.05$  km/s at 41 s (Fig. 2c, see Text S1 for discussions on  
173 the location error).

174 We applied the same analysis to the R2 signal and found that it exhibits little dispersion between periods of 23 s  
175 and 39 s, with a nearly constant group velocity of  $2.90$  km/s  $\pm$   $0.01$  km/s (Fig. 2d). It is worth mentioning that the  
176 uncertainty of the R2 group velocity is much smaller (less than one-fifth) than that of R1 due to its longer travel time  
177 (See Text S1 for details).

178 Fig. 2b shows that R3 is significantly affected by a glitch. Nevertheless, based on the deglitched data, the multiple  
179 filter analysis shows little dispersion and a nearly constant group velocity of about  $2.90$  km/s  $\pm$   $0.02$  km/s (Fig. S3).  
180 This similar value of the R2 and R3 group velocities confirms the reliability of the R2 measurements given their  
181 similar paths (i.e., they share the same path for about 19,000 km or about 80% of the R3 path length).

### 182 **3.2 Inversion Along the R1 Path**

183 We inverted the group velocity measurements to constrain the average seismic velocity profile along the R1 path  
184 using a Niche Genetic Algorithm (Koper et al., 1999; Li et al., 2021) to sample different possible models and the CPS  
185 code package (Herrmann, 2013) to calculate the group velocities predicted by these models at different periods.

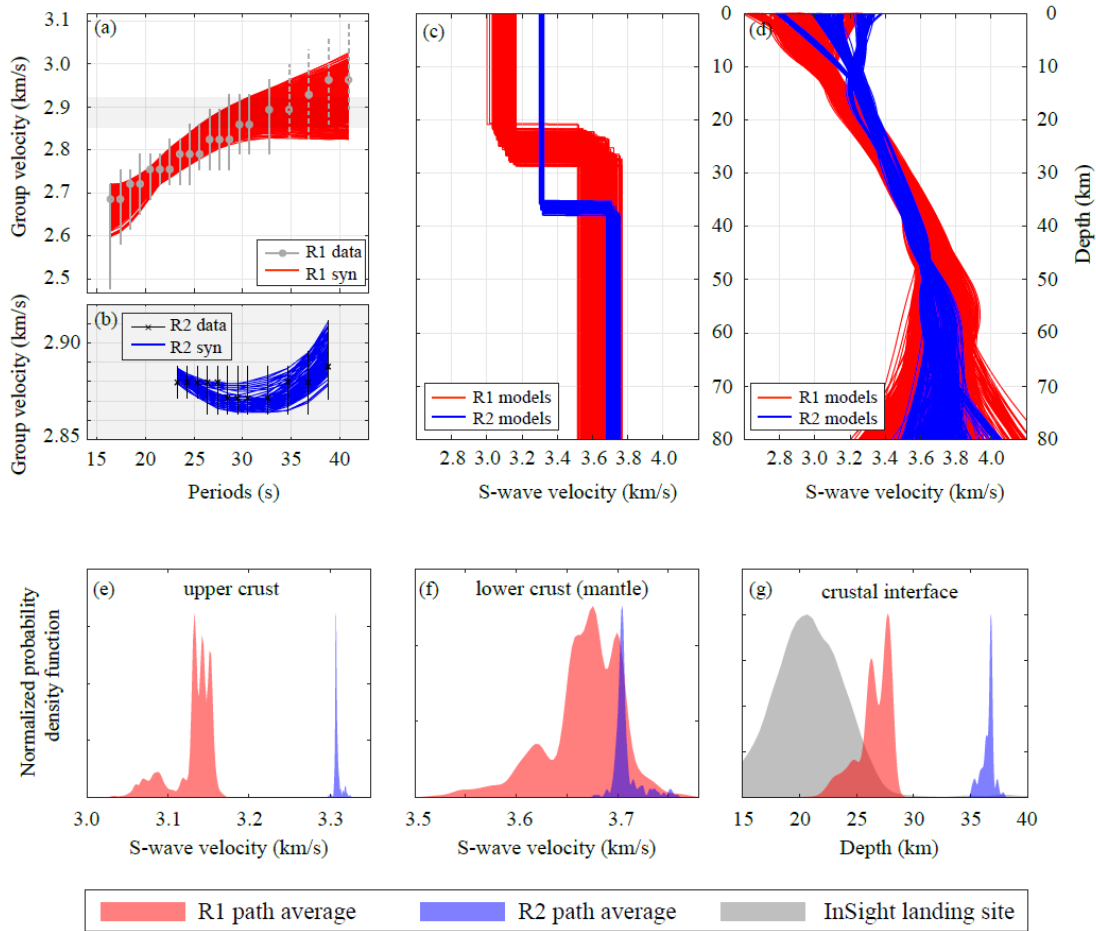
186 We chose to represent the model with a layered crustal parameterization because previous receiver function studies

187 (Lognonné et al., 2020; Kim et al., 2021; Knapmeyer-Endrun et al., 2021) exhibited the presence of sharp interfaces  
188 in the crust. In addition, we preferred to set the number of layers to two because this model setting with only three  
189 free parameters (i.e., the depth of the interface, and the shear-wave velocities above and below this interface) is less  
190 likely prone to overfitting the data. If this simplified model fails to fit the observed group velocities, we can then  
191 consider a more complex model. Based on the sensitivity curves of the Rayleigh waves at periods shorter than 40 s  
192 (Fig. S4), we only constrained the structure above 80 km depth. At greater depths, we used the values of the  
193 InSight\_KKS21GP model (Knapmeyer-Endrun et al., 2021; Khan et al., 2021; Stähler et al., 2021a and 2021b), which  
194 was constructed from teleseismic body waves (See Text S2 for the model setup). We also tested a smoothed model  
195 setting with eight third-order B-splines (Fig. 3d) and found that the average velocities above (or below) the interface  
196 are similar between the discontinuity and the smoothed model settings (Fig. S5).

197 Fig. 3c shows that a simplified model with two layers in the top 80 km can reproduce the R1 dispersion curve.  
198 Specifically, the shear-wave velocity is estimated to be 3.05 - 3.17 km/s in the top layer, and 3.50 - 3.78 km/s in the  
199 bottom layer. The interface depth estimation is 21 - 29 km. Fig. 3f shows that the depth of the inverted interface along  
200 the R1 path overlaps with the depth of the intra-crustal interface beneath the InSight lander constrained by the receiver  
201 function (Knapmeyer-Endrun et al., 2021), although the mean value deviates (possibly due to the difference in the  
202 regions to which those two methods are sensitive).

203 We note that Knapmeyer-Endrun et al. (2021) provided two possible crustal thicknesses beneath the lander: a  
204 thinner crustal model with a shallow Moho depth of  $20 \pm 5$  km, and a thicker crustal model (where the interface at  
205 around 20 km is interpreted as an intra-crustal interface) with a deeper Moho depth of  $39 \pm 8$  km (though with a  
206 smaller impedance contrast across this deeper Moho). Here, we prefer to refer to the interface at 21- 29 km (inverted  
207 in this study) as the intra-crustal interface since subsequent studies from Kim et al. (2021) and Durán et al. (2022)  
208 favored the thicker crustal scenario. We also want to note that we cannot resolve the deeper Moho (if it exists) since  
209 only the discontinuity with the most significant velocity jump will be detected with the current one-interface setting.

210



211

212

213 **Figure 3.**

- 214 (a) Group velocity measurements (grey circles), uncertainties (vertical bars), and synthetic group velocity dispersion  
 215 curves (in red, corresponding to the models shown in (c) with the same color) along the R1 path. The range of  
 216 the y-axis (i.e., group velocity) in the shaded gray region is the same as that in (b).  
 217 (b) Similar to (a), but for the R2 path, and the corresponding models (in blue) shown in (c).  
 218 (c) Shear-wave velocity profiles for all the acceptable models along the R1 (in red) and R2 (in blue) paths from the  
 219 inversion for the discontinuity model setting.  
 220 (d) Similar to (c), but for the smoothed (i.e., third-order B-splines) model setting.  
 221 (e) Normalized probability density functions of the shear-wave velocities in the upper crust for all the acceptable  
 222 models (R1 models in red, and R2 models in blue) in (c).  
 223 (f) Similar to (e), but for the shear-wave velocities in the lower crust and mantle (i.e., down to 80 km).  
 224 (g) Similar to (e), but for the depth of the crustal interface. The probability density function in gray shows the depth  
 225 of the base of the intra-crustal discontinuity beneath the lander from the receiver function study (Knappmeyer-  
 226 Endrun et al., 2021).

227

228

229

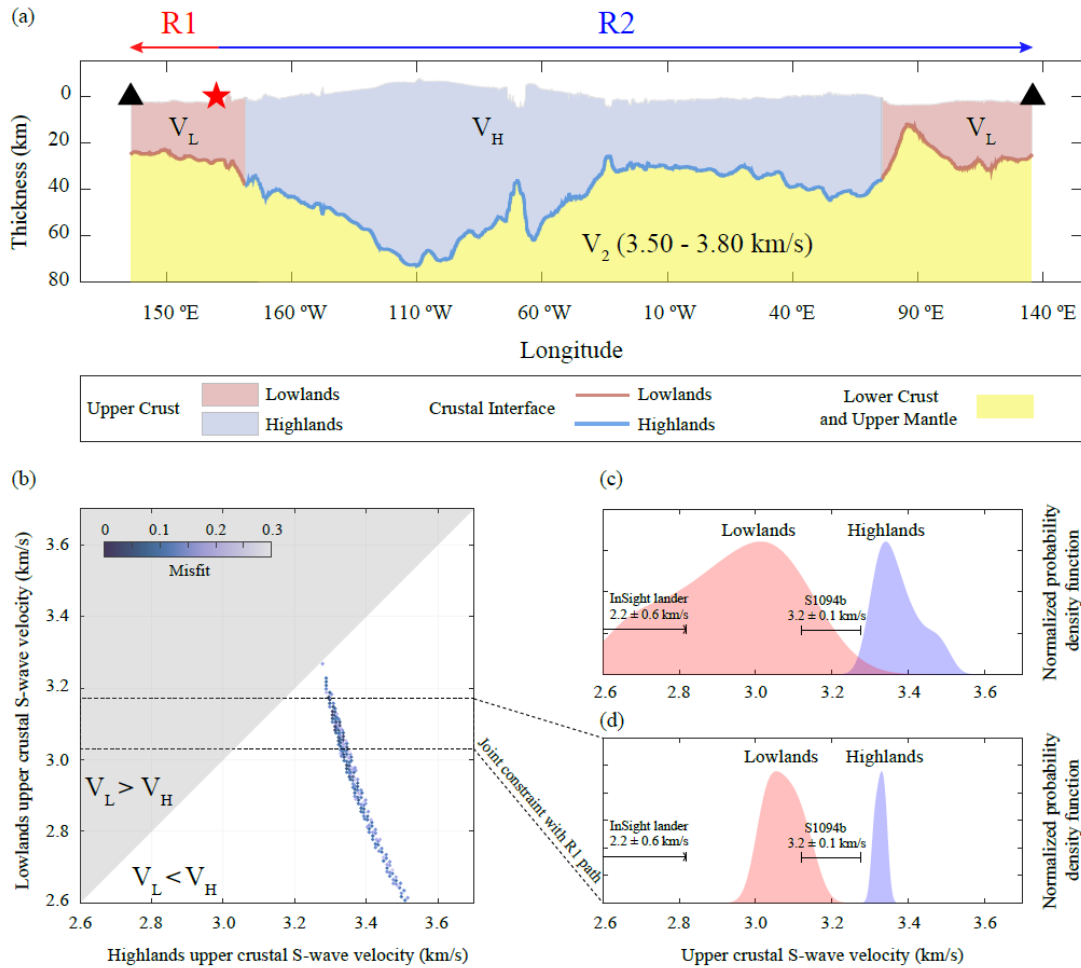
### 230 **3.3 Inversion Along the R2 Path**

231 We note that it is reasonable to perform the inversion with a representative one-layer model along the entirety of  
232 the R1 path since there are few topographic changes (e.g., Fig. 4a). However, along the R2 path, it may be preferable  
233 to account for the significant lateral variations in both topography and crustal thickness (Wieczorek et al., 2022),  
234 rather than simply using an average one-layer model (e.g., Fig. 3c) to explain the R2 dispersion curve in Fig. 3b.

235 We thus divided the R2 path into 3,230 sub-paths, and within each sub-path (of which the length is shorter than  
236 the wavelength) we can assume a one-layer model with a similar setup as for R1. The upper crustal thickness models  
237 along the R2 path are modified from Wieczorek et al. (2022) as prior information (See Text S3 for the R2 model  
238 setup). There are only three free parameters in the R2 inversion, i.e., the upper crustal shear-wave velocities in the  
239 lowlands ( $V_L$ ) and highlands ( $V_H$ ), and the shear-wave velocity below the crustal interface ( $V_2$ ).

240 Grid search results show that within the given range of  $V_2$  (i.e., 3.50 - 3.78 km/s from the R1 inversion results in  
241 Fig. 3e), a series of models (Fig. 4b), with upper crustal velocities of 2.61 - 3.27 km/s in the lowlands and 3.28 - 3.52  
242 km/s in the highlands, can fit the R2 measurements (Fig. S6).

243 The probability density functions in Fig. 4c illustrate that the upper crustal shear-wave velocity in the highlands  
244 (i.e., 3.28 - 3.52 km/s) is systematically faster than that in the lowlands (i.e., 2.61 - 3.27 km/s). We further reduced  
245 the number of acceptable models from the R2 inversion with the extra constraint from the R1 inversion (i.e., upper  
246 crustal velocity in the lowlands should be in the range of 3.05 - 3.17 km/s). The down-selected models, which satisfy  
247 both the R1 and R2 observations, also demonstrate a greater upper crustal shear-wave velocity in the highlands (i.e.,  
248 3.17 - 3.33 km/s) than that in the lowlands (i.e., 3.05 - 3.17 km/s).



249

250

251 **Figure 4.**

252 (a) Model setup for the R2 inversion. The upper crustal thickness models modified from Wieczorek et al. (2022) are  
 253 used as prior information and fixed in the inversion. Along the R2 path, the only three free parameters are the  
 254 upper crustal shear-wave velocities in the lowlands ( $V_L$ ) and highlands ( $V_H$ ), and the shear-wave velocity ( $V_2$ )  
 255 below the crustal interface (See Text S3 for the R2 model setup).

256 (b) Grid search results for the upper crustal shear-wave velocity in the lowlands ( $V_L$ , the y-axis), and the upper  
 257 crustal shear-wave velocity in the highlands ( $V_H$ , the x-axis) along the R2 path. The acceptable models that can  
 258 fit the R2 measurements are shown as filled circles, with color scales corresponding to the misfits (See Text S2  
 259 for the misfit function). The dashed region indicates where the models also satisfy the R1 observations (i.e., an  
 260 upper crustal shear-wave velocity of 3.05 - 3.17 km/s in the lowlands). The shaded gray area to the left of the  
 261 diagonal indicates the region where the upper crustal velocity in the lowlands is faster than that in the highlands.  
 262 Note that at each grid point, a grid search for the shear-wave velocity below the crustal interface ( $V_2$ ) is also  
 263 performed.

264 (c) Normalized probability functions of the upper crustal shear-wave velocities (lowlands models are in red, and  
 265 highlands models are in blue) for the acceptable models in (b). S-wave velocities beneath the InSight lander (in  
 266 the depth range of ~8 - 20 km, Knappmeyer-Endrun et al., 2021) and along the great circle path from the meteorite  
 267 impact S1094b (Kim et al., 2022) are also annotated.

268 (d) Similar to (c), but for the models that satisfy both the R1 and R2 observations (i.e., in the dashed region in (b)).

269

## 270 **4. Discussion**

### 271 **4.1 Comparison with the InSight landing site**

272 The most sensitive depth range of the Rayleigh waves analyzed is from  $\sim 10$  to 50 km (Fig. S7), though there are  
273 also a few sensitivities to greater depths. Therefore, we have better constraints on the upper crust (i.e., above the  
274 crustal interface), than the lower crust and mantle.

275 Since Lognonné et al. (2020) and Knapmeyer-Endrun et al. (2021) obtained the first Martian crustal structure  
276 beneath the InSight landing site, whether it represents local geologies or global features has been debated. In the  
277 similar depth range of  $\sim 8 - 20$  km, beneath the lander, the S-wave velocity is estimated to be  $2.2 \pm 0.6$  km/s  
278 (Knapmeyer-Endrun et al., 2021). This upper crustal velocity beneath the lander (also located in the lowlands) is  
279 significantly smaller than the average velocity (i.e.,  $\sim 3$  km/s, see Fig. 4c and d) along the surface wave path in the  
280 lowlands.

281 Similar S-wave velocity (i.e.,  $\sim 3.2$  km/s) of the upper crust in the lowlands (along the surface wave path from a  
282 meteorite impact) has also been recently reported (Kim et al., 2022). This faster velocity has been attributed to the  
283 different compositions and/or reduced porosity in the volcanic areas along the path (Kim et al., 2022).

284 For marsquake S1222a, the surface wave path also likely traverses the volcanic units in the lowlands (Fig. S8).  
285 Therefore, the crustal porosity may have been occluded or obscured by later magmatism (e.g., Wilson and Head,  
286 1994), resulting in a faster S-wave velocity than beneath the lander (where there are higher porosities).

### 287 **4.2 Upper Crust in the Lowlands and the Highlands**

288 The upper crust velocity in the lowlands, though larger than the InSight landing site, is systematically smaller than  
289 that in the highlands (Fig. 4c and d). Possible interpretations for the smaller upper crustal shear-wave velocity values  
290 in the lowlands than in the highlands could include some combination of differing compositions, reductions in  
291 porosity at depth, and/or the presence of sedimentary rocks.

292 Variations in lithology and rock compositions are a common major cause of regional variations in crustal seismic  
293 structure (Rudnick and Fountain, 1995). The Martian crust is thought to be of basaltic composition on average (Taylor  
294 and McLennan, 2009). Recently, using global crustal thickness and thermal evolution models, Thiriet et al. (2018)  
295 suggested that felsic rocks were more common in the Noachian-dominated southern highlands, leading to an average

296 bulk density of  $480 \text{ kg/m}^3$  less than the northern lowland crust. However, this density difference should lead to lower,  
297 rather than higher, seismic velocities (for a wide range of lithologies, e.g., Brocher, 2005) in the highlands.

298 Compositional differences could also affect the thermal regime and thus have an indirect influence on seismic  
299 velocities. For example, a more differentiated southern highland crust would also be characterized by higher  
300 abundances of heat-producing elements (Thiriet et al., 2018; Wieczorek et al., 2022) and, when coupled with a thicker  
301 crust, higher heat flow (e.g., Hahn et al., 2011; Parro et al., 2017). A distinctive crustal thermal regime could lead to  
302 very different depth-dependent porosity behavior.

303 Porosity can also significantly affect the seismic wave speed such that higher porosity results in lower shear-wave  
304 velocity (e.g., Manga and Wright 2021). Both compaction and viscous deformation will result in porosity reduction  
305 with depth. Gyalay et al. (2020) showed that the closure of pore space should occur over a narrow depth range of a  
306 few kilometers and all porosity should have been removed for depths greater than about 12-23 km (Wieczorek et al.  
307 2022). Accordingly, in the highlands, where the upper crust is thicker on average (Fig. 4a) and surface heat flow is  
308 greater (Hahn et al., 2011; Parro et al., 2017), a larger proportion of the upper crust may lie beneath depths where  
309 porosity has been lost, leading to shear-wave velocities that are higher than in the northern lowlands when averaged  
310 over the thickness of the upper crust interrogated by the R2 paths.

311 To quantitatively assess the influence of porosity, we assumed that the velocity difference between the lowlands  
312 and highlands is affected by porosity alone. With a pore closure depth of 23 km (Wieczorek et al. 2022) and an aspect  
313 ratio of 0.1 (Heap, 2019), the velocity difference can be explained by a porosity reduction of 8 - 15% (Fig. S9, see  
314 Text S4 for details).

315 The presence of thick accumulations of sedimentary rocks could also lead to lower density (and thus, for a wide  
316 range of lithologies, low shear-wave velocities, e.g., Brocher, 2005) due to a variety of features/processes, including  
317 the presence of elevated primary porosity for poorly consolidated and/or weakly cemented sedimentary rocks;  
318 secondary porosity for diagenetically altered sedimentary rocks; low-density hydrated alteration phases, such as  
319 phyllosilicates and amorphous silica, formed during chemical weathering and/or diagenesis (McLennan & Grotzinger,  
320 2008; McLennan et al., 2019). However, for most locations on Mars, sedimentary rock thicknesses are on the order  
321 of a few kilometers at most (e.g., Grotzinger et al., 2015; Grotzinger and Milliken, 2012; Bradley et al., 2002).  
322 Therefore, based on our current knowledge of the total sedimentary mass and its distribution on Mars (e.g., McLennan,  
323 2012, Grotzinger and Milliken, 2012), the presence of sedimentary rocks alone probably cannot explain the lower  
324 upper crustal shear-wave velocity in the lowlands, where the crustal interface is located at  $\sim 26 \text{ km}$ .

### 325 **4.3 R2 Group Velocity**

326 Another major difference between the group velocity along R1 and R2 is that there is positive dispersion along R1  
327 but there is almost no dispersion along R2. We found that for a typical velocity model derived for the highlands,  
328 where the upper crustal thickness is greater than in the lowlands, the group velocity exhibits negative dispersion.  
329 Therefore, the negative dispersion in the highlands (Fig. S7e) could cancel out the positive dispersion in the lowlands  
330 (Fig. S7d), yielding little dispersion along the R2 path.

331 However, it is worth noting that long-period pressure-induced signals are also present in seismic data (Kenda et  
332 al., 2020; Stutzmann et al., 2021) and are carried by the environmental wind, resulting in an apparent burst of noise  
333 without dispersion. Given the relatively low signal-to-noise ratio for R2 and R3, this absence of dispersion could also  
334 be an artifact of the wind noise.

## 335 **5. Conclusion**

336 We have observed two minor-arcs (R1, and R3) and one major-arc (R2) Rayleigh wave generated by the largest  
337 marsquake ever recorded. The group velocities along the R1 path increase from  $2.70 \pm 0.05$  km/s to  $2.95 \pm 0.05$  km/s  
338 between periods of 17 s and 42 s and can be explained by a two-layer model with a crustal interface depth of 21 - 29  
339 km and an upper crustal shear-wave velocity of 3.05 - 3.17 km/s in the lowlands. The group velocity along the R2  
340 path exhibits a nearly constant value of 2.90 km/s and can be explained by upper crustal thickness models constrained  
341 from gravity data and upper crustal shear-wave velocities of 2.61 - 3.27 km/s and 3.28 - 3.52 km/s in the lowlands  
342 and highlands, respectively. The lower shear-wave velocity in the lowlands compared to that in the highlands may be  
343 due to the presence of thick accumulations of sedimentary rocks, and relatively higher porosity.

344

345

346

347

## 348 **Acknowledgments**

349 J.L. and C.B. were supported by NASA InSight PSP grant #80NSSC18K1679 and S. M. McLennan by NASA



350 InSight PSP grant #80NSSC18K1622. P.L. and M.W. are supported by Agence Nationale de la Recherche (MAGIS,  
351 ANR-19-CE31-0008-08; IdEx Université Paris Cité, ANR-18-IDEX-0001) and by CNES for SEIS science support.

352 This is InSight Contribution Number 278. InSight seismic data presented here  
353 ([http://dx.doi.org/10.18715/SEIS.INSIGHT.XB\\_2016](http://dx.doi.org/10.18715/SEIS.INSIGHT.XB_2016)) are publicly available through the Planetary Data System  
354 (PDS) Geosciences node (InSight SEIS Data Bundle, 2021), the Incorporated Research Institutions for Seismology  
355 (IRIS) Data Management Center under network code XB and through the Data center of Institut de Physique du  
356 Globe, Paris. We acknowledge NASA, CNES, their partner agencies and Institutions (UKSA, SSO, DLR, JPL, IPGP-  
357 CNRS, ETHZ, IC, MPS-MPG), and the flight operations team at JPL, SISMOC, MSDS, IRIS-DMC, and PDS for  
358 providing SEED SEIS data.

## 359 **Conflict of Interest**

360 The authors declare no conflicts of interest relevant to this study.

## 361 **Open Research**

362 The datasets used in this study are achieved and released by InSight Mars SEIS Data Service and are  
363 available to the science community (InSight Mars SEIS Data Service, 2019; InSight Marsquake Service,  
364 2022). Data sets (both the raw data and the deglitched data in SAC format, after removing the instrument  
365 response) for this research are available on the Zenodo repository: <https://doi.org/10.5281/zenodo.7325555>.  
366 The InSight\_KKS21GP model is available on the IPGP Data Center (doi: 10.18715/IPGP.2021.kpmqrmz8).

## 367 **References**

368 Andrews-Hanna, J.C., Zuber, M.T. and Banerdt, W.B., 2008. The Borealis basin and the origin of  
369 the Martian crustal dichotomy. *Nature*, 453(7199), pp.1212-1215.  
370 Banerdt, W.B., Smrekar, S.E., Banfield, D., Giardini, D., Golombek, M., Johnson, C.L., Lognonné,

371 P., Spiga, A., Spohn, T., Perrin, C. and Stähler, S.C., 2020. Initial results from the InSight mission  
372 on Mars. *Nature Geoscience*, 13(3), pp.183-189.

373 *Beghein et al., 2022. Evidence for Large-Scale Seismic Anisotropy in the Martian Crust from*  
374 *Surface Waves (submitted to the GRL S1222a special issue).*

375 Bradley, B. A., Sakimoto, S. E., Frey, H., Zimbelman, J. R., 2002. Medusae Fossae Formation:  
376 New perspectives from Mars Global Surveyor. *Journal of Geophysical Research – Planets*, 107,  
377 E85050, doi:10.1029/2001JE001537.

378 Brocher, T. M. (2005) Empirical relations between elastic wavespeeds and density in the Earth's  
379 crust. *Bull. Seis. Soc. Amer.*, 95, 2081-2092.

380 Clinton, J. F., Ceylan, S., van Driel, M., Giardini, D., Stähler, S. C., Böse, M., Charalambous, C.,  
381 Dahmen, N. L., Horleston, A., Kawamura, T., et al., 2021. The marsquake catalogue from  
382 InSight, sols 0–478, *Physics of the Earth and Planetary Interiors*, 310, 106595.

383 Compaire, N., Margerin, L., Garcia, R. F., Pinot, B., Calvet, M., Orhand-  
384 Mainsant, G., Kim, D., Lekic, V., Tauzin, B., Schimmel, M., et al., 2021. Autocorrelation of  
385 the ground vibrations recorded by the seis-insight seismometer on mars, *Journal of Geophysical*  
386 *Research: Planets*, 126(4), e2020JE006498.

387 Drilleau, M., Samuel, H., Garcia, R. F., Rivoldini, A., Perrin, C., Michaut, C., Wieczorek, M.,  
388 Tauzin, B., Connolly, J. A. D., Meyer, P., Lognonné, P., & Banerdt, W. B. (2022). Marsquake  
389 locations and 1-D seismic models for Mars from InSight data. *Journal of Geophysical Research:*  
390 *Planets*, 127, e2021JE007067.

391 Durán, C., A. Khan, S. Ceylan, G. Zenhäusern, S. Stähler, J. F. Clinton, and D. Giardini.  
392 "Seismology on Mars: An analysis of direct, reflected, and converted seismic body waves with  
393 implications for interior structure." *Physics of the Earth and Planetary Interiors* 325 (2022): 106851.

394 Frey, H.V., 2006. Impact constraints on the age and origin of the lowlands of Mars. *Geophysical*  
395 *Research Letters*, 33(8).

396 Garcia, Raphael F., et al. "Newly formed craters on Mars located using seismic and acoustic  
397 wave data from InSight." *Nature Geoscience* (2022): 1-7.

398 Grotzinger, J. P., Gupta, S., Malin, M. C., Rubin, D. M., Schieber, J. et al. (2015) Deposition,  
399 exhumation, and paleoclimate of an ancient lake deposit, Gale Crater, Mars. *Science*, 350,  
400 aac7575, doi:10.1126/science.aac7575.

401 Grotzinger, J. P., Milliken, R. E., 2012. The sedimentary rock record of Mars: Distribution,  
402 origins, and global stratigraphy. In: J. P. Grotzinger and R. E. Milliken (eds.) *Mars*  
403 *Sedimentology*, SEPM Spec. Publ. 102, 1-48.

404 Gyalay, S., Nimmo, F., Plesa, A.-C., Wieczorek, M., 2020. Constraints on thermal history of  
405 Mars from depth of pore closure below InSight. *Geophysical Research Letters*, 47,  
406 e2020GI088653.

407 Heap, M. J. (2019). P-and S-wave velocity of dry, water-saturated, and frozen basalt:  
408 Implications for the interpretation of Martian seismic data. *Icarus*, 330, 11-15.

409 Herrmann, R.B., 2013. Computer programs in seismology: An evolving tool for instruction and  
410 research. *Seismological Research Letters*, 84(6), pp.1081-1088.

411 InSight Mars SEIS Data Service. (2019). SEIS raw data, Insight Mission. IPGP, JPL, CNES, ETHZ,  
412 ICL, MPS, ISAE-Supaero, LPG, MFSC. [https://doi.org/10.18715/SEIS.INSIGHT.XB\\_2016](https://doi.org/10.18715/SEIS.INSIGHT.XB_2016)

413 InSight Marsquake Service (2022). Mars Seismic Catalogue, InSight Mission; V12 2022-10-01.  
414 ETHZ, IPGP, JPL, ICL, Univ. Bristol. <https://doi.org/10.12686/a18>

415 InSight SEIS Data Bundle. 2021. PDS Geosciences (GEO) Node.  
416 Kawamura et al., 2022. Largest Marsquake Ever Detected by InSight: S1222a. (submitted to the  
417 GRL S1222a special issue, attached).  
418 Kenda, B., Drilleau, M., Garcia, R.F., Kawamura, T., Murdoch, N., Compaire, N., Lognonné, P.,  
419 Spiga, A., Widmer - Schnidrig, R., Delage, P. and Ansan, V., 2020. Subsurface structure at the  
420 InSight landing site from compliance measurements by seismic and meteorological experiments.  
421 Journal of Geophysical Research: Planets, 125(6), p.e2020JE006387.  
422 Khan, A., Ceylan, S., van Driel, M., Giardini, D., Lognonné, P., Samuel, H., Schmerr, N.C.,  
423 Stähler, S.C., Duran, A.C., Huang, Q. and Kim, D., 2021. Upper mantle structure of Mars from  
424 InSight seismic data. Science, 373(6553), pp.434-438.  
425 Kim, D., Lekić, V., Irving, J.C., Schmerr, N., Knapmeyer - Endrun, B., Joshi, R., Panning, M.P.,  
426 Tauzin, B., Karakostas, F., Maguire, R. and Huang, Q., 2021. Improving constraints on planetary  
427 interiors with PPS receiver functions. Journal of Geophysical Research: Planets, 126(11),  
428 p.e2021JE006983.  
429 Kim, D., Banerdt, W.B., Ceylan, S., Giardini, D., Lekić, V., Lognonné, P., Beghein, C., Beucler,  
430 É., Carrasco, S., Charalambous, C. and Clinton, J., 2022. Surface waves and crustal structure on  
431 Mars. Science, 378(6618), pp.417-421.  
432 Knapmeyer-Endrun, B., Panning, M. P., Bissig, F., Joshi, R., Khan, A., Kim, D., Lekic, V.,  
433 Tauzin, B., Tharimena, S., Plasman, M., et al., 2021. Thickness and structure of the martian crust  
434 from InSight seismic data, Science, 373(6553), 438–443.  
435 Koper, K.D., Wyssession, M.E. and Wiens, D.A., 1999. Multimodal function optimization with a  
436 niching genetic algorithm: A seismological example. Bulletin of the Seismological Society of  
437 America, 89(4), pp.978-988.  
438 Li, J., Beghein, C., Wookey, J., Davis, P., Lognonné, P., Schimmel, M., Stutzmann, E.,  
439 Golombek, M., Montagner, J.P. and Banerdt, W.B., 2022a. Evidence for crustal seismic  
440 anisotropy at the InSight lander site. Earth and Planetary Science Letters, 593, p.117654.  
441 Li, J., Beghein, C., Davis, P., Wiczorek, M.A., McLennan, S.M., Kim, D., Lekić, V., Golombek,  
442 M., Schimmel, M., Stutzmann, E. and Lognonné, P., 2022b. Crustal Structure Constraints from  
443 the Detection of the SsPp Phase on Mars. Earth and Space Science, p.e2022EA002416.  
444 Li et al., 2022c. Second Seismic Anchor Point of the Martian Crustal Structure Away From the  
445 InSight Landing Site. Nature Communications (under review, 10.21203/rs.3.rs-1829147/v1).  
446 Li, J., Beghein, C., et al., 2022d. Data for "Different Martian Crustal Seismic Velocities across  
447 the Dichotomy Boundary from Multi-Orbiting Surface Waves". Zenodo.  
448 <https://doi.org/10.5281/zenodo.7325555>  
449 Li, J., Chen, M., Koper, K.D., Zhou, T., Xi, Z., Li, S. and Li, G., 2021. FastTrip: A Fast MPI -  
450 Accelerated 1D Triplexation Waveform Inversion Package for Constraining Mantle Transition  
451 Zone Discontinuities. Seismological Research Letters, 92(4), pp.2647-2656.  
452 Lognonné, P., Banerdt, W.B., Giardini, D., Pike, W.T., Christensen, U., Laudet, P., De Raucourt,  
453 S., Zweifel, P., Calcutt, S., Bierwirth, M. and Hurst, K.J., 2019. SEIS: InSight's seismic  
454 experiment for internal structure of Mars. Space Science Reviews, 215(1).  
455 Lognonné, P., Banerdt, W., Pike, W., Giardini, D., Christensen, U., Garcia, R. F., Kawamura, T.,  
456 Kedar, S., Knapmeyer-Endrun, B., Margerin, L., et al., 2020. Constraints on the shallow elastic and  
457 anelastic structure of Mars from InSight seismic data, Nature Geoscience, 13(3), 213–220.

458 Marinova, M.M., Aharonson, O. and Asphaug, E., 2008. Mega-impact formation of the Mars  
459 hemispheric dichotomy. *Nature*, 453(7199), pp.1216-1219.

460 McLennan, S., & Grotzinger, J., 2008. The sedimentary rock cycle of Mars. In J. Bell (Ed.), *The*  
461 *Martian Surface: Composition, Mineralogy and Physical Properties* (Cambridge Planetary  
462 Science, pp. 541-577). Cambridge: Cambridge University Press.

463 McLennan, S. M., 2012. Geochemistry of sedimentary processes on Mars. In: J. P. Grotzinger  
464 and R. E. Milliken (eds.) *Mars Sedimentology*, SEPM Spec. Publ. 102, 119-138.

465 McLennan, S.M., Grotzinger, J.P., Hurowitz, J.A. and Tosca, N.J., 2019. The sedimentary cycle  
466 on early Mars. *Annual Review of Earth and Planetary Sciences*, 47, pp.91-118.

467 Panning, M.P., Beucler, É., Drilleau, M., Mocquet, A., Lognonné, P. and Banerdt, W.B., 2015.  
468 Verifying single-station seismic approaches using Earth-based data: Preparation for data return  
469 from the InSight mission to Mars. *Icarus*, 248, pp.230-242.

470 *Panning et al., 2022. Locating the largest event observed on Mars with multi-orbit surface waves*  
471 *(submitted to the GRL S1222a special issue, attached).*

472 Parro, L. M., Jiménez-Díaz, Mansilla, F. and Ruiz, J. (2017) Present-day heat flow models of  
473 Mars. *Sci. Rept.*, 7, 45629.

474 Posiolova, L.V., Lognonné, P., Banerdt, W.B., Clinton, J., Collins, G.S., Kawamura, T., Ceylan,  
475 S., Daubar, I.J., Fernando, B., Froment, M. and Giardini, D., 2022. Largest recent impact craters  
476 on Mars: Orbital imaging and surface seismic co-investigation. *Science*, 378(6618), pp.412-417.

477 Rudnick, R. L. and Fountain, D. M. (1995) Nature and composition of the continental crust: A  
478 lower crustal perspective. *Rev. Geophys.*, 33, 267-309.

479 Schimmel, M., Stutzmann, E., Lognonné, P., Compaire, N., Davis, P., Drilleau, M., Garcia, R.,  
480 Kim, D., Knapmeyer-Endrun, B., Lekic, V., et al., 2021. Seismic noise autocorrelations on Mars,  
481 *Earth and Space Science*, p. e2021EA001755.

482 Scholz, J.-R., Widmer-Schmidrig, R., Davis, P., Lognonné, P., Pinot, B., Garcia, R. F., Hurst, K.,  
483 Pou, L., Nimmo, F., Barkaoui, S., et al., 2020. Detection, analysis, and removal of glitches from  
484 InSight's seismic data from Mars, *Earth and Space Science*, 7(11), e2020EA001317.

485 Smith, D.E., Zuber, M.T., Frey, H.V., Garvin, J.B., Head, J.W., Muhleman, D.O., Pettengill, G.H.,  
486 Phillips, R.J., Solomon, S.C., Zwally, H.J. and Banerdt, W.B., 2001. Mars Orbiter Laser  
487 Altimeter: Experiment summary after the first year of global mapping of Mars. *Journal of*  
488 *Geophysical Research: Planets*, 106(E10), pp.23689-23722.

489 Stähler, S. C., Khan, A., Banerdt, W. B., Lognonné, P., Giardini, D., Ceylan, S., Drilleau, M.,  
490 Duran, A. C., Garcia, R. F., Huang, Q., et al., 2021a. Seismic detection of the martian core,  
491 *Science*, 373(6553), 443–448.

492 Stähler et al., 2021b. Interior Models of Mars from inversion of seismic body waves (Version  
493 1.0). IGP Data Center;

494 Stutzmann, É., Schimmel, M., Lognonné, P., Horleston, A., Ceylan, S., van Driel, M., Stähler, S.,  
495 Banerdt, B., Calvet, M., Charalambous, C. and Clinton, J., 2021. The polarization of ambient  
496 noise on Mars. *Journal of Geophysical Research: Planets*, 126(1), p.e2020JE006545.

497 Tanaka, K.L., Skinner Jr, J.A., Dohm, J.M., Irwin III, R.P., Kolb, E.J., Fortezzo, C.M., Platz, T.,  
498 Michael, G.G. and Hare, T.M., 2014. Geologic map of Mars.

499 Taylor, S. R. and McLennan, S. M. (2009) *Planetary Crusts: Their Composition, Origin and*  
500 *Evolution*. Cambridge Univ. Press (Cambridge), 378pp.

501 Trampert, J. and Woodhouse, J.H., 1996. High resolution global phase velocity distributions.  
502 Geophysical research letters, 23(1), pp.21-24.

503 Thiriet, M., Michaut, C., Breuer, D. and Plesa, A.-C. (2018) Hemispheric dichotomy in  
504 lithospheric thickness on Mars caused by differences in crustal structure and composition. J.  
505 Geophys. Res. – Planets, 123, 823-848.

506 Wieczorek, M.A., Broquet, A., McLennan, S.M., Rivoldini, A., Golombek, M., Antonangeli, D.,  
507 Beghein, C., Giardini, D., Gudkova, T., Gyalay, S. and Johnson, C.L., 2022. InSight constraints  
508 on the global character of the Martian crust. Journal of Geophysical Research: Planets,  
509 p.e2022JE007298.

510 Xu, Z., Stutzmann, E., Lognonné, P., Schimmel, M., Montagner, J.-P., and Kawamura, T.: Radial  
511 anisotropy from surface-wave observation in Mars, Europlanet Science Congress 2022, Granada,  
512 Spain, 18–23 Sep 2022, EPSC2022-863, <https://doi.org/10.5194/epsc2022-863>.

513 Zhong, S. and Zuber, M.T., 2001. Degree-1 mantle convection and the crustal dichotomy on  
514 Mars. Earth and Planetary Science Letters, 189(1-2), pp.75-84.

515 Zhou, Y., Dahlen, F.A. and Nolet, G., 2004. Three - dimensional sensitivity kernels for surface  
516 wave observables. Geophysical Journal International, 158(1), pp.142-168.

517